Numerical analysis of factors influencing freely falling annular disks in an infinite fluid

Dianfang Bi (毕殿方)⊙

School of Aerospace Engineering, Tsinghua University, Beijing 100084, China
and School of Astronautics, Harbin Institute of Technology, Harbin, Heilongjiang 150001, China

Jiaxing Lu (卢佳兴)⊙ and Yingjie Wei (魏英杰)⊙*
School of Astronautics, Harbin Institute of Technology, Harbin, Heilongjiang 150001, China

Tiezhi Sun (孙铁志)
School of Naval Architecture and Ocean Engineering, Dalian University of Technology, Dalian, Liaoning 116024, China

This work presents a numerical investigation of the dynamics of freely falling annular disks released from still in infinite water. Based on the large eddy simulation, a dynamic fluid body interaction model and moving computational method are utilized to obtain the full six degrees of freedom of the disks. In particular, we performed a comprehensive analysis of the influencing factors on the falling styles of the disks, i.e., the inner to outer diameter ratio ($0 \leqslant \eta \leqslant 0.9$), the dimensionless moment of inertia ($4 \times 10^{-4} \leqslant I^* \leqslant 4.2 \times 10^{-4}$) and the body to fluid density ratio ($1.2 \leqslant \rho^* \leqslant 6$). η is found to be a key parameter for the falling trajectory and the corresponding flow structures, with $\eta = 0.6$ as a turning point from regular to random motion. From low to high I^*, although the disks still exhibit hula-hoop (HH) motion, the dispersion degree of each period and the fluid forces against the disk's inertia increase gradually. We find that regardless of ρ^*, the disk trajectory exhibits HH motion, while more discrete vortices are generated for heavy disks. Ultimately, the mechanism of the planar precession of HH motion is explained by combining the time evolution of horizontal displacement, fluid forces, and vortical structures. Consequently, a hysteresis effect is observed during falling.

I. INTRODUCTION

Since it was first discussed by Newton [1], bodies freely falling or rising in a fluid have been an intriguing phenomenon in nature and industry. The fluttering of falling leaves from trees [2], the spreading of seeds (samara) [3], the oscillatory paths of bubbles rising in water [4,5], and hailstone growth in the atmosphere [6] are common examples in nature with classic nonstraight trajectories and unsteady fluid flows. Cummins *et al.* [7] investigated the flight of dandelion seeds, in which case a highly effective structure can help seed dispersal over formidable distances. Furthermore, inspired by wind-dispersal seeds, distributed collections of elaborate miniaturized three-dimensional (3D) fliers can be designed by optimizing the interaction between the device and the surrounding air [8]. Understanding the mechanism of path instabilities involves the complex fluid-structure interaction

*yingjiewei@hit.edu.cn

(FSI) problem. It is widely realized that the object's size, shape, inertia, and surrounding flow properties play significant roles in governing the trajectories and wake structures. These factors control the relative intensity between the solid and fluid, which in turn gives rise to path and wake instability.

The vast variety of investigations on freely moving objects in fluid have been devoted to particles, spheres, cylinders, cones, and disks [9–12], from which various motion types can be observed. Ern *et al.* [13] reviewed the different objects rising or settling in fluids from the point of combining the path and wake instability. Among these objects with distinct geometrical features, disks are studied widely due to their various falling styles by simply changing the geometrical parameters. Generally, there are five material parameters and three derived dimensionless parameters to define a moving disk in fluid: the disk diameter d, thickness e, density ρ_d, fluid density ρ_f, kinematic viscosity ν, dimensionless moment of inertia $I^* = \pi \rho_d / 64 \rho_f \lambda$, diameter-to-thickness ratio, λ, and Reynolds number Re $= Ud/\nu$ [14,15], where ν is the kinematic viscosity. The classical falling phase diagram as a function of the dimensionless moment of inertia I^* and Reynolds number was divided into four sections [15]: steady falling, periodic, tumbling, and chaotic. With the increment of Re and I^*, different falling motions were observed, from steady falling to the final chaotic motions.

Most of the experimental studies mainly focused on the planar motion of the moving bodies due to the limitation of the measurement methods. Zhong *et al.* [16] investigated the time evolution of a free thin disk motion with six degrees of freedom for the first time and defined two new nonplanar types of disks with much smaller I^*: transitional and spiral motions. Their following work revealed that the initial release angle could only affect when the transition occurred, but the disks with the same parameters remain in the same motion mode [17]. Previous studies on disks have implicitly involved an assumption that the disk thickness could be ignored when $\lambda \geqslant 10$, i.e., thin disks. Auguste *et al.* [18] found that the influence of λ cannot be ignored at low Re when viscosity was dominant in the flows. However, regardless of the λ of the disk, it is widely acknowledged that the disk usually exhibits a nonlinear path. Interestingly, Heisinger *et al.* [19] plotted the probability density function maps of the disk landing site for all the different falling types by dropping the disks repeatedly and found that, contrary to intuition, the location directly below the drop point was the least probable landing site except for the steady motion.

Disk topologies and flow conditions are considered to reveal various types of falling patterns and the corresponding flow structures. Kim *et al.* [20] investigated experimentally a pair of rigidly linked disks and identified a novel falling motion characterized by a helical path with conical configurations but for different oscillation amplitudes for the upper and lower disks. Inspired by the parachuting flight of porous wings of many insects and plant seeds, the bristles were found to have the ability to stabilize the falling trajectories when mounted on circular disks in a wide range of Reynolds numbers due to the formation of symmetric vortical structures close to the disk center [21]. For a heterogeneous disk with an eccentric void, a new stable descending motion with large eccentricity was observed to fall with an extremely large inclination angle [22]. The previous studies mainly focused on the rigid disks; however, according to the research by Verhille [23], the flexible disk exhibited a U shape with a maximum curvature in the center, and two regimes, i.e., rigid and flexible regimes, existed under different shape factors. As regards the surrounding flow conditions, Esteban *et al.* [24] found that the mean falling velocity of a finite-size disk increases in homogeneous turbulence compared to that in quiescent flow. The disks falling in a stratified two-layer fluid can undergo distinct settling scenarios caused by a fluid density jump [25]. However, considering a linearly stratified fluid, the disk may experience three phases before reaching its gravitational equilibrium level, from broadside-on to edgewise settling and finally returning to broadside orientation [26].

Clearly, if the disk has a hole in the center, it is expected that the path instability and wake structure will change dramatically [27]. It has been proven that for fixed porous disks, which are widely encountered in many scientific and industrial applications, such as flame holders [28], minimizing the pressure loss [29] and dealing with the flow of wind turbines [30] or parachutes [31], the disk porosity can cause drastic changes in the near-wake flow topology compared to disks with no perforation layout [32]. An important new dimensionless parameter is introduced for the

annular disk: the inner to outer diameter ratio $\eta = d/D$, where d and D are the two diameters of the annular disk. Moffatt [27] suggested that the falling motions and wake structures would be quite different when involving complex phenomena, such as the interaction between the inner and outer edges, which can lead to collisions and twists of the generated vortices. For freely moving disks with holes in the center, a stabilization process is observed from tumbling to fluttering when increasing the hole size [33]. Different from the solid disks, a new counter-rotating vortex ring is formed at the inner edge of the disks, which can exert torques on the disk to offset the effects of the unstable outer vortex. Therefore, central holes stabilized the falling motion of the disks. However, this kind of stabilization effect did not always work on low-density annular disks. No typical stable falling motions were observed for disks with a density ratio of 1.18, which is lower than the existing studies, as the authors' previous experimental work pointed out [34]. The classical straight vertical path was superimposed by a random lateral vibration for a larger inner to outer diameter ratio η. When η was smaller, the path exhibited irregular movement. From low to moderate η, full regular 3D motions could be observed. Furthermore, proper orthogonal decomposition (POD) analysis utilizing the experimental data revealed that the first POD mode contained the most energy of the flow field, and the second POD mode controlled the turbulence of the flow field [35].

In view of previous studies, there is a need for further investigations on the influencing factors on the falling trajectories and vortical structures of annular disks, which are responsible for the changes in movement and orientation of the body. The authors' previous experimental investigations [34,35] illuminated that the central hole has significant effects on the falling trajectory and focused on new falling patterns but lacked a systematic exploration of the influencing factors of the geometric parameters due to the limitation of the experimental facilities. Compared to the experimental study, the numerical method is a more appropriate technique that can provide an infinite fluid region, allowing full development of the body and covering a wide range of the parameter space.

With the rising of the microelectromechanical system (MEMS), wind-dispersal microfliers with various types of layout topology have taken flight. Among these microfliers, Iyer *et al.* [36] takes advantage of the characteristics of porous disks to achieve aerodynamic stability and prolong traveling distance, and compares the trajectory to a solid disk of an unstable descent. As a potential layout for future microfliers, the annular disk can provide a novel strategy to stabilize the falling motion, and the research work, however, remains relatively scarce. In the present work, based on a well-established numerical method, three main dimensionless parameters, the inner to outer diameter ratio η, the dimensionless moment of inertia I^*, and the body-to-fluid-density ratio ρ^*, are studied in detail to provide a comprehensive understanding of the dynamic behaviors of annular disks. It has been proved that for freely falling solid disks, the second critical Reynolds number where Hopf bifurcation takes place is about 118 [37], beyond which large-scale and periodic shedding vortical structures are dominant. Thus, the Reynolds numbers in the current study range approximately from 550 to 800, which are higher than the bifurcation threshold to avoid flow transitions and reduce the effects of Reynolds numbers. The current investigation is focused on the characteristics of the interaction between the evolution of vortical structures and the corresponding falling trajectories. The remainder of this paper is organized as follows: Details of the mathematical model and simulations are described in Sec. II A. Then, the simulation methods are validated in Sec. II C. The results are presented in Sec. III. Finally, this paper concludes in Sec. IV.

II. NUMERICAL FORMULATION

A. Mathematical model

Consider an annular disk with outer and inner diameters D and d, respectively, moving in a viscous fluid. For an incompressible Newtonian fluid with density ρ_f and viscosity μ, the flow is governed by the following continuity and Navier-Stokes (NS) equations:

$$\frac{\partial \rho_f}{\partial t} + \nabla \cdot (\rho_f \mathbf{v}) = 0, \tag{1}$$

$$\frac{\partial \rho_f \mathbf{v}}{\partial t} + \nabla \cdot (\rho_f \mathbf{v}\mathbf{v}) = -\nabla p + \nabla \cdot \tau, \tag{2}$$

where the stress tensor τ is

$$\tau_{ij} = \mu \left(\frac{\partial v_i}{\partial x_j} + \frac{\partial v_j}{\partial x_i} - \frac{2}{3}\delta_{ij}\frac{\partial v_k}{\partial x_k} \right). \tag{3}$$

The NS equations are discretized using the finite volume method based on the commercial computational fluid dynamics code STAR-CCM+, which has been widely utilized to solve the problems of freely moving objects [38,39]. The treatment of turbulence entails using large eddy simulation (LES) to resolve as many vortical structures as possible since vortex motion is a critical aspect of the study. The wall-adapting local-eddy viscosity (WALE) is employed for the subgrid scale model, which requires less computational resources and is more suitable for near walls. The subgrid scale turbulent viscosity μ_t is

$$\mu_t = \rho_f \Delta^2 S_w, \tag{4}$$

where Δ is the length scale defined as $\min(\kappa s, C_w V^{1/3})$ with κ the von Kármán constant at a value of 0.41, s the distance to the wall, $C_w = 0.544$ the model coefficient, and V the cell volume. S_w is the deformation parameter defined as

$$S_w = \frac{\mathbf{S}_d : \mathbf{S}_d^{3/2}}{\mathbf{S}_d : \mathbf{S}_d^{5/4} + \mathbf{S} : \mathbf{S}^{5/2}}, \tag{5}$$

where $\mathbf{S}$ is the mean strain rate tensor given by $0.5(\nabla \bar{\mathbf{v}} + \nabla \bar{\mathbf{v}}^T)$. $\mathbf{S}_d$ is defined as

$$\mathbf{S}_d = \frac{1}{2}[\nabla \mathbf{v} \cdot \nabla \mathbf{v} + (\nabla \mathbf{v} \cdot \nabla \mathbf{v})^T] - \frac{1}{3}\mathrm{tr}(\nabla \mathbf{v} \cdot \nabla \mathbf{v})\mathbf{I} \tag{6}$$

with $\mathbf{I}$ the identity tensor.

To ensure temporal and spatial fidelity for good LES results, it is important to achieve a convective Courant number with a value below 1 in the domain of interest. An implicit unsteady solver is used for the transient computation, and second-order temporal discretization that provides the option of doing a second-order time discretization with five time levels (one current time level and previous four time levels) is employed to improve the accuracy of this relatively low Reynolds number flow. The convective term is discretized by a second-order upwind scheme. The numerical algorithm is based on the semi-implicit method for pressure-linked equation (SIMPLE) scheme to solve the discretized system of equations for pressure-velocity coupling.

The six-degree-of-freedom (6DOF) solver is employed to solve the free motion of the disks:

$$m\frac{d\mathbf{v}}{dt} = \mathbf{f}, \tag{7}$$

$$\mathbf{M}\frac{d\omega}{dt} + \omega \times \mathbf{M}\omega = \mathbf{n}, \tag{8}$$

where m and $\mathbf{M}$ are the mass and tensor moment of inertia of the disk, $\mathbf{v}$ and ω are the translational and angular velocity of the disk center, and $\mathbf{f}$ and $\mathbf{n}$ are the resultant force and moment acting on the disk:

$$\mathbf{f} = \mathbf{f_p} + \mathbf{f}_\tau + \mathbf{f}_g, \tag{9}$$

$$\mathbf{n} = \mathbf{n}_p + \mathbf{n}_\tau, \tag{10}$$

where $\mathbf{f}_g = m\mathbf{g}$ is the gravity force, $\mathbf{f}_p$ and $\mathbf{n}_p$ are the fluid pressure force and moment acting on the disk, respectively, and $\mathbf{f}_\tau$ and $\mathbf{n}_\tau$ are the fluid shear force and moment, respectively.

The 6DOF solver computes the fluid forces, moments, and gravitational forces on the disk. For the motion of the disk, a dynamic fluid body interaction (DFBI) model is used, where pressure
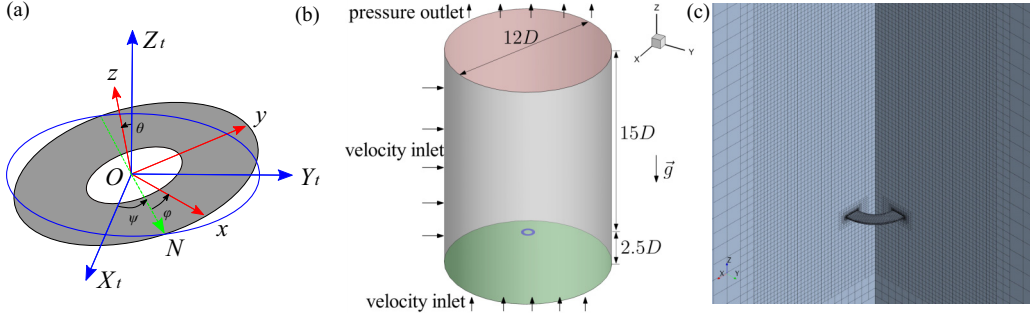
FIG. 1. (a) The coordinate systems describing the position and orientation of the 6DOF disk throughout the simulation; the translation coordinate (in blue), O-$X_tY_tZ_t$; the disk local coordinate system (in red), O-xyz; and ψ for precession angle, θ for nutation angle, and ϕ for intrinsic rotation angle. (b) Schematic of the computational domain and boundary conditions; a zero velocity inlet is prescribed at the bottom and side of the domain to simulate an infinite fluid and the whole domain moves and rotates with the disk. (c) A cutaway view of the grid structure.

and shear forces are integrated over the surfaces. The initial angular and translational velocities are set equal to zero, and the rotation axis of the disk is vertically upwards. The series of parameters regarding the falling trajectory and force evolution are monitored during the simulation, including the disk's centroid and angular position, translational and angular velocities, pressure, and shear forces.

B. Computational model and grid

In the current study, the aspect ratio λ is larger than 10; thus, the effects of the thickness can be ignored, i.e., the thin disk hypothesis is applied to this work. Three dimensionless parameters are investigated: inner to outer diameter ratio η, dimensionless moment of inertia I^*, and body to fluid density ratio ρ^*. In order to isolate the effect of one parameter each time, we hold the other two dimensionless parameters constant by varying the physical sizes (inner and outer diameters, thickness) of the disks simultaneously. The outer diameter D ranges from 24 to 80 mm while keeping the thin disk hypothesis. The disk is released from still in an infinite water region with density $\rho_f = 999$ kg/s and viscosity $\mu = 0.0015$ Pa s. The coordinate system used in the simulation is shown in Fig. 1(a). The translation coordinate (in blue), O-$X_tY_tZ_t$, is at the center of the disk and coincides with the laboratory coordinate, O-XYZ, at the initial position, and the directions of the axis remain the same as those of the O-XYZ system. The disk local coordinate system (in red), O-xyz, is fixed in the disk's center of mass, translating and rotating with the disk. The line of nodes N (in green) is defined as the intersection of the planes xy and X_tY_t. Three Euler angles, ψ for precession, θ for nutation, and ϕ for intrinsic rotation, are utilized to denote the rotation of the disk.

A cylindrical domain of diameter $D_c = 12D$ is set for the freely falling disk, and the domain extends $2.5D$ and $15D$ along the Z direction from the center of the disk, as shown in Fig. 1(b). The effect of the domain size has been properly evaluated in Refs. [40,41], which allows the full development of the wake behind the disk. The whole computational domain translates and rotates at a velocity the same as that of the disk, which is known as the moving computational domain (MCD) method [42]. Thus, an infinite fluid domain is created rather than constructing an extremely long computational domain [39]. The computational domain is separated into sets of unstructured trimmed cells as a cutaway view of the grid shown in Fig. 1(c). To accurately capture steep gradients, the mesh is refined in the zone close to the surface of the disk to ensure $y+$ below 1. From a base mesh size that is linked to the specific disk diameter and mean falling velocity, the finest mesh gradually grows to the coarsest mesh near the outermost part of the domain. On the disk surface, a
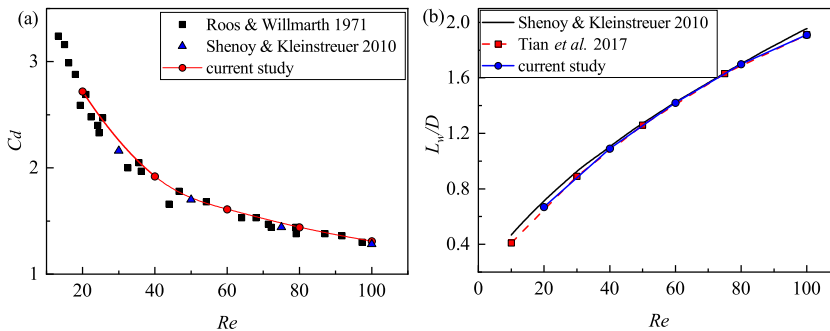
FIG. 2. Comparisons of the results for the steady flow over a circular disk (Tian *et al.* [41], Shenoy and Kleinstreuer [43], Roos and Willmarth [44]) with an aspect ratio $\lambda = 10$: (a) drag coefficient; (b) wake length.

nonslip boundary is imposed for the velocity, and the pressure is set to a zero normal gradient. At the inlet and side of the domain, the velocity inlet boundary is set to create a quiescent fluid. For the outlet of the domain, the velocity is prescribed as a zero normal gradient, and the pressure is set as zero.

C. Numerical validation

To validate the numerical approach, first, calculations of flow around a stationary disk with an aspect ratio $\lambda = 10$ are conducted. The simulation is set up following Shenoy and Kleinstreuer [43], where the drag coefficient C_d in the axial direction and wake length L_w behind the disk are computed from Re = 10 to Re = 100. L_w is the streamwise distance from the disk center to the position where the streamwise flow changes its direction [41], i.e., the streamwise length of the recirculation area. For the current validation analysis, a uniform incoming flow is perpendicular to the surface of the stationary disk. The simulation is run for a sufficient number of iterations until a satisfying convergence is achieved when the values of C_d and L_w are no longer varied and reach an asymptotic limit. As shown in Fig. 2(a), the drag coefficient shows good agreement with the direct numerical simulation (DNS) results reported by Shenoy and Kleinstreuer [43] and the experimental measurements by Roos and Willmarth [44]. For the wake length, the adopted method also maintains favorable performance compared to the studies by Shenoy and Kleinstreuer [43] and Tian *et al.* [41]. For freely falling disks, as reported by Bi *et al.* [34], even for identical release conditions, the trajectory of an annular disk exhibits different trajectories but the same statistical characteristics due to the inherent uncertainty of the fluid-structure system. The same phenomenon also appears in the simulation studies. Therefore, to verify the capability of the current approach, the statistical parameters of the falling trajectory of a typical 3D hula-hoop (HH) motion are compared, such as oscillating Strouhal number St and standard deviation σ of displacement in the X and Y directions in the horizontal plane and average vertical falling velocity $\bar{U}_z$. The results are shown in Table I and compared to the experimental research [34], where a large number of disks were released in a water tank from still. Both the 1D motion (cases E1 and S1) and fully developed 3D motions (cases E2 and S2, and E3 and S3) were compared. The statistical quantities of the trajectory show that marginal differences can be observed from the experiments and simulations.

Furthermore, Table II presents the mesh sensitivity analysis by using various numbers of grids from cases M1 to M4. With an increasing number of grids, the results agree well with the experimental data with very small variations. The temporal resolutions of the current method are also studied and summarized in Table III with different time steps. Considering the accuracy of the simulations and computing resources, a grid size of 740 781 and time step 0.0016 are employed in the current study.

TABLE I. Comparison of trajectory parameters to the experimental results of Bi *et al.* [34]. Case E1 is a one-dimensional (1D) motion of a disk falling vertically with $I^* = 5 \times 10^{-4}$ and $\eta = 0.93$. Cases E2 and E3 are fully developed 3D motions with E2, $I^* = 9 \times 10^{-4}$ and $\eta = 0.6$, and E3, $I^* = 6 \times 10^{-4}$ and $\eta = 0.33$. Cases S1, S2, and S3 are the corresponding numerical cases. The unit of $\bar{U}_z$ is (m/s).

| | | 1D motion | | 3D motion | | | |
	Direction	E1	S1	E2	S2	E3	S3
St	X			0.31	0.31	0.43	0.47
	Y			0.31	0.31	0.43	0.47
σ	X			0.027	0.027	0.0090	0.0093
	Y			0.025	0.027	0.0099	0.0097
$|\bar{U}_z|$	Z	0.079	0.081	0.033	0.033	0.021	0.022

Overall, the present numerical scheme can yield reliable results against the available experimental data and thus is valid for the simulation of falling annular disks.

III. RESULTS

On the basis of the numerical method established in the previous section, this section deeply explores the factors that affect the falling trajectories and flow field structure of the annular disks. We focus on the stabilization effect of the inner to outer diameter ratio η, the influence of the dimensionless moment of inertia I^* on the rotating movement, and the relative magnitude of inertial effects defined by body to fluid density ratios ρ^*. Furthermore, the mechanisms of planar precession of the commonly encountered HH motion are discussed by associating the paths and vortical characteristics.

A. Inner to outer diameter ratio η

Apparently, the most prominent feature of an annular disk is the central hole compared to the solid disk, which in turn can lead to a completely different flow field and the corresponding falling path, as suggested by Moffatt [27]. It is conceivable that when the size of the center hole is very small, i.e., there is very low porosity, there would be negligible differences between the annular and solid disks. However, when high porosity is encountered, the annular disk can be regarded as a flat ring. Therefore, it can be reasonably inferred that the inner to outer diameter ratio η is an important parameter that affects the disk movement and fluid flow. In this section, we keep a constant dimensionless moment of inertia $I^* = 7 \times 10^{-4}$ and body to fluid density ratio $\rho^* = 1.2$ and analyze the influence of η on the falling trajectory and flow structures. I^* and ρ^* are controlled

TABLE II. Comparison of trajectory parameters and mesh independence of a freely falling annular disk. Case M3 corresponds to case S2 in Table I.

	Direction	E2	M1	M2	M3 (S2)	M4
Elements			204 797	385 101	740 781	1 056 015
ΔT_z			0.0008	0.0008	0.0008	0.0008
St	X	0.31	0.32	0.31	0.31	0.31
	Y	0.31	0.32	0.31	0.31	0.31
σ	X	0.027	0.026	0.026	0.027	0.027
	Y	0.025	0.029	0.026	0.027	0.028
$|\bar{U}_z|$	Z	0.033	0.034	0.035	0.035	0.034

TABLE III. Comparison of trajectory parameters and time step independence of a freely falling annular disk.

	Direction	E2	M4	M3 (S2)	M5	M6
Elements			740 781	740 781	740 781	740 781
ΔT_z			0.0004	0.0008	0.0016	0.0023
St	X	0.31	0.31	0.31	0.31	0.31
	Y	0.31	0.31	0.31	0.31	0.31
σ	X	0.027	0.027	0.027	0.028	0.028
	Y	0.025	0.027	0.027	0.027	0.027
$|\bar{U}_z|$	Z	0.033	0.035	0.035	0.035	0.035

at relatively low values to create a strong disk-fluid coupling system where η can play an important role in altering the falling mode. As listed in Table IV, the Reynolds number Re_{U_z} experiences a sudden change after $\eta = 0.6$. Within the whole range of η, Re_{U_z} is below 800, and the flow field remains in a laminar flow state without a large-scale transition to turbulent structures.

With a drastic change between $\eta = 0.6$ and $\eta = 0.7$, a potential falling style transition occurs, which is confirmed in Fig. 3, showing the horizontal two-dimensional (2D) trajectories of the annular disks at different η values from 0 to 0.9. The annular disks at $0 \leqslant \eta \leqslant 0.6$ present a HH motion that was first defined by Auguste et al. [18] for a solid disk as a zigzagging motion in which the plane of the successive zigzags slowly precessed about the vertical axis and was later observed by the experimental study for an annular disk [34]. When $\eta > 0.6$, the horizontal trajectories of the disk become irregular with no definite shapes, indicating that the uncertainty of falling motion increases. Different from the chaotic motion characterized by randomly alternate tumbling and oscillating behaviors at relatively large Re and I^* reported by Field et al. [15], the disks do not flip but keep moving back and forth in the lateral direction through all parameter space. Hence, the motion of the disks at $\eta > 0.6$ is defined as lateral irregular (LI) motion. Compared to the solid disk at $\eta = 0$, the trajectories are less affected by the central hole when $\eta \leqslant 0.6$, and all of the disks under $\eta \leqslant 0.6$ share the same horizontal characteristics.

Figure 4 presents the mean translation and mean velocity of the disk on the horizontal plane with the increment of η, where the error bands in the figure represent the fluctuation range defined by the standard deviation of the corresponding parameters. With the increment of η, the mean amplitude of horizontal translation does not appear to have an evident regularity, nor does the fluctuation range. When $\eta = 0.9$, the horizontal movement amplitude and fluctuation range of the disk are obviously increased compared with other conditions. When the disks are within the HH regime, the horizontal velocity decreases slowly with increasing η. However, for $\eta > 0.6$, the mean velocity decreases rapidly, and the oscillation of the horizontal velocity also decreases. Vincent et al. [33] discussed the stabilization effects of the central holes of the annular disks with relatively large density. In contrast, from the phenomenon observed above, the stabilization process does not apply to the cases for the whole range of η because the inertia and the fluid force of the disks are very close.

$\eta = 0.6$ is a turning point from HH motion to LI motion, during which the angle of attack and fluid force also exhibit disparate characteristics, as shown in Fig. 5. The angle of attack is defined as the line-face angle between the disk surface and the velocity vector. By this definition, the angle of attack is $90°$ at the beginning stage of the falling process when the orientation is unchanged.

TABLE IV. The inner to outer diameter ratio η and the corresponding Reynolds number Re_{U_z}. I^* and ρ^* are kept at 7×10^{-4} and 1.2, respectively.

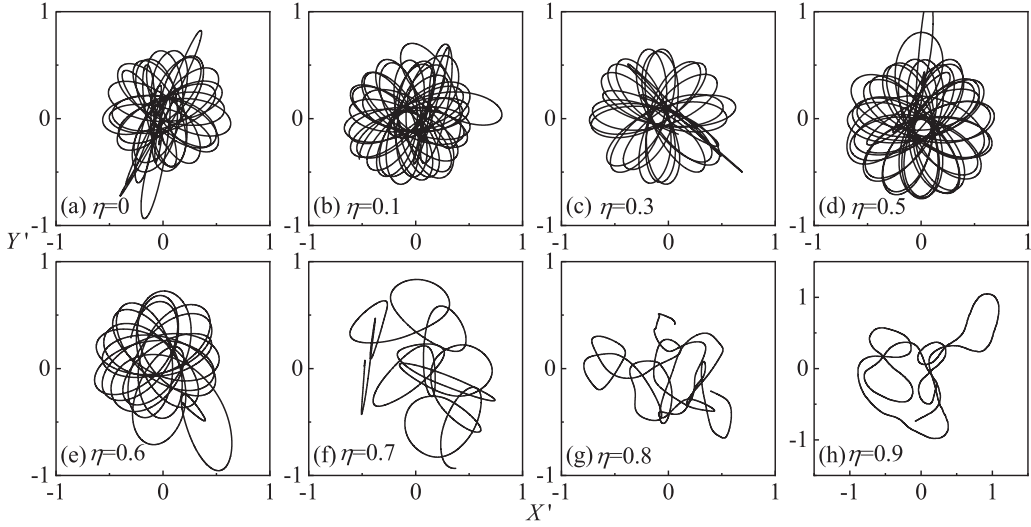| η	0	0.1	0.3	0.5	0.6	0.7	0.8	0.9
Re_{U_z}	801	748	700	608	582	638	688	740

FIG. 3. The horizontal trajectories of the annular disks at different η from 0 as a solid disk to 0.9 as a flat ring. The coordinates are nondimensionalized by outer diameter D. See also videos S1, S2, and S3 of the Supplemental Material [45] for the disks at $\eta = 0$, 0.5, and 0.9.
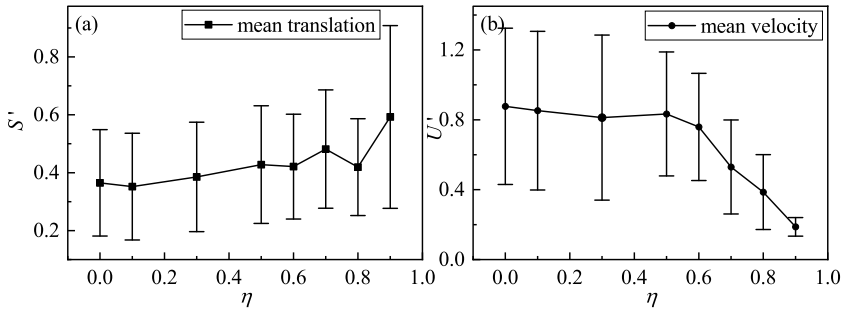

FIG. 4. The mean translation and velocity in the horizontal plane of the disks at different η. S' and U' are nondimensionalized by the outer diameter D and mean vertical falling velocity $\bar{U}_z$, respectively. The error bands denote the fluctuation range of the parameters.
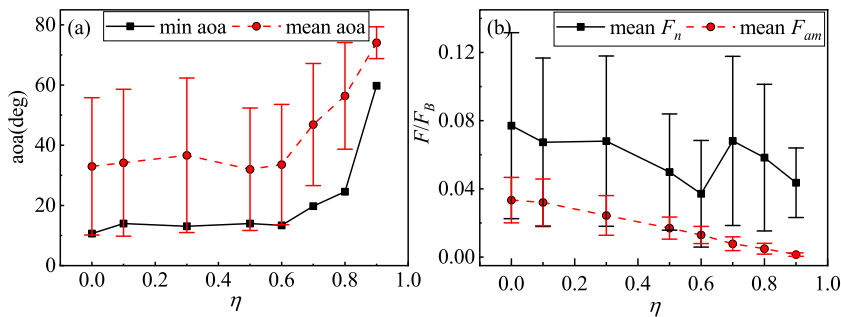
FIG. 5. (a) The mean and minimum angle of attack. (b) The mean normal fluid force and added-mass force of the disks at different η. The fluid forces are nondimensionalized by the disk buoyancy force $F_B = \rho_f g V$, with V the volume of the disk.
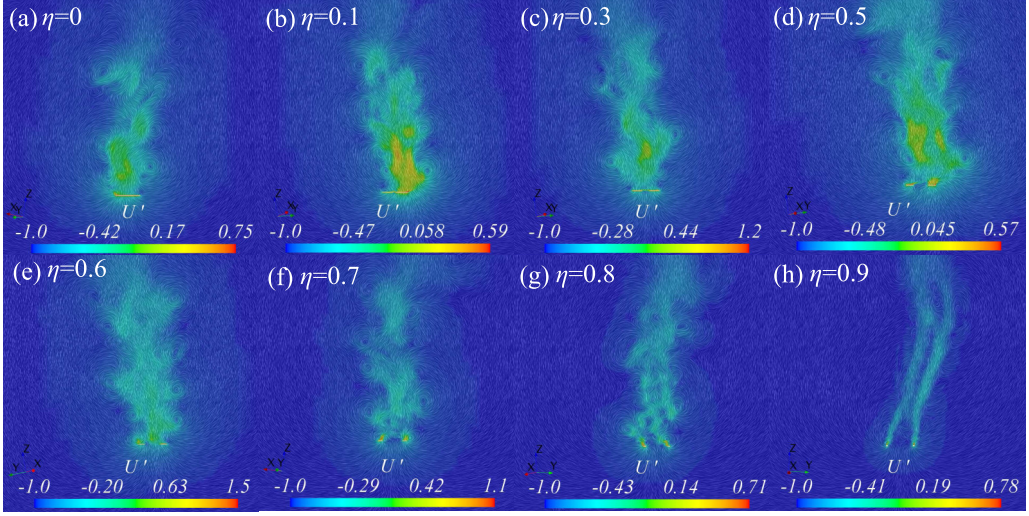
FIG. 6. The instantaneous velocity vector fields represented by line integral convolution (LIC) maps at different η values from 0 to 0.9. The velocity magnitude is nondimensionalized as $U' = (U - \bar{U}_z)/|\bar{U}_z|$. The symmetry loss of the outer staggered vortices and small discrete vortices leads to irregular falling trajectories at high η.

The total fluid forces exerted on the disk are decomposed into the normal force F_n, providing the centripetal force for the semielliptical planar trajectory and the added-mass force F_{am}, where $F_{am} = -C_{am}\rho_f \frac{d\mathbf{U}}{dt}$. The derivation procedure of the added-mass coefficient C_{am} is included in the Appendix. The minimum and mean angles of attack are consistent with the change of η during the falling process, with an evident rise after $\eta = 0.6$. The fluid force acting on the disk is primarily responsible for the different motion patterns of the disk. The added-mass force F_{am} decreases approximately linearly with the increment of η, as well as the fluctuation range of F_{am}, which can be readily understood because the added-mass effect is related to the shape of the body and the volume of the disk is reduced with η. The normal force F_n provides less centripetal force for the HH motion due to lighter weight of the disk, but higher or equal F_n can be found for LI motion because the horizontal trajectories of LI motion consist of more sharp turning as depicted in Fig. 3.

The corresponding analysis and visualization of the wakes reveal the different characteristics of the falling styles from $\eta = 0$ to $\eta = 0.9$, as instantaneous velocity vector fields are represented by the line integral convolution (LIC) maps in the cross-section plane in Fig. 6. LIC was first introduced by Cabral and Leedom [46] for visualizing imaging vector fields by convoluting a white noise image along streamlines computed from the vector field and is capable of visualizing the vector field at a satisfactory resolution. Most of the computational domain remains undisturbed, and vortices only occur along the falling path of the disk. A series of staggered vortices are generated at the disk's outer rim and gradually decay and become unrecognizable at more than five times the disk diameter. These staggered vortices are distributed nearly symmetrically along the vertical moving direction, which can offset the inertia effects of the disk, but the symmetry is lost with the increment of η and the falling styles switch to LI motion. At the extreme condition of $\eta = 0.9$, however, the scale of small discrete vortices is equivalent to the characteristic length of the disk, which cannot exert stable fluid forces on the disk.

At high η above 0.7, wake instability has been a key factor for the occurrence of LI motion, which resembles the "regime A" observed with spheres, two-dimensional cylinders, and thin disks, as described by Ern *et al.* [13]. However, in the current study, the amplitude of the irregular transverse movements is usually on the same order of the disk's outer diameter as shown above, much larger
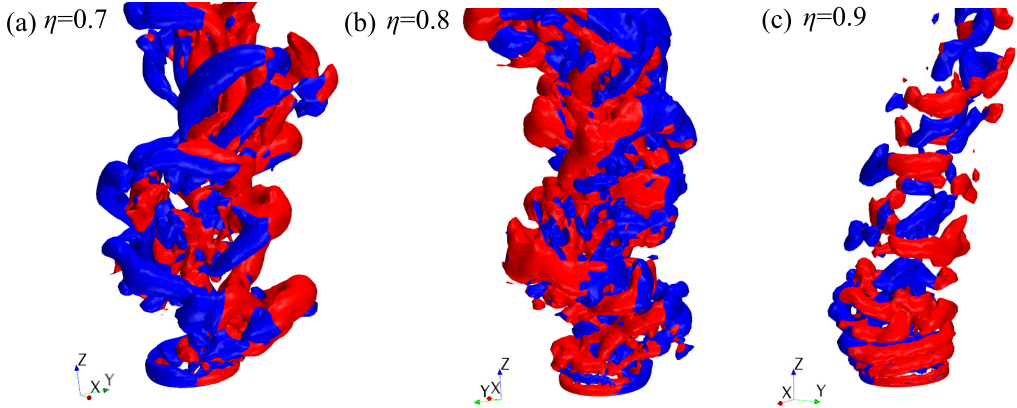
FIG. 7. The instantaneous wake structures of the disks at $\eta = 0.7$, 0.8, and 0.9 after the flow is fully developed. The vortical structures are visualized by the Q isosurface at $Q = 0.1$, and the colors red and blue denote the positive and negative vorticity along the x axis, respectively.

than "regime A," which lacks in-depth investigations of the flow structures. In particular, Fig. 7 shows the instantaneous 3D wake structures of the flow field at LI motion, where η ranges from 0.7, 0.8, and 0.9. Clearly, with the increment of η, the large-scale regular vortical structure is broken into more discrete small-scale vortices, and the twisted double-threaded vortices lose their inherent structures and become vortex rings. The vortex rings detach from the surface of the disk as soon as they are generated at both the inner and outer edges of the disk, nearly without the attachment and development process. The shedding point seems randomly distributed on the disk; therefore, the asymmetrical fluid forces caused by the shedding vortex rings drive the disk into an irregular state in the horizontal plane.

To study the reason for the onset of the wake instability, figure 8 shows the LIC maps at different moments from the beginning of the falling process. When the disks start to move from being released, the incoming fluid flows over the outer edges of the disk and forms an initial outer counter-rotating vortex pair (OCRVP), denoted by Γ_o. For the annular disks at $\eta = 0.5$ and $\eta = 0.9$, another inner counter-rotating vortex pair (ICRVP) Γ_i is formed to balance the effects of the OCRVP. The OCRVP attaches to the outer edges throughout the initial process; however, the ICRVP sheds periodically from the inner edge and dissipates gradually into the wakes. In contrast, a secondary vortex pair is induced by the large-scale outer vortices downstream of the wake, which has limited effects on the movement of the disk. However, due to the nature of the fluid, the motion of the vortex pairs does not always remain stable, and slight perturbance can be magnified, which in turn exerts unstable forces on the disks. For the annular disk of $\eta = 0.9$, the relative intensity of the inner and outer vortex pair becomes comparable, and the interaction between them is stronger. For all three cases in Fig. 8, as time elapses, vortices begin to form on the inner and outer edges of the disk, and the instability of the flow causes the vortices to fall off.

To quantitatively demonstrate the instability process, Fig. 9 shows the velocity circulation that can indicate the intensity of the vortex varying with η before the onset of the wake instability and the whole time evolution of velocity circulation at $\eta = 0$, 0.5, and 0.9. The integral curve is a circular curve so that the center of the circular curve coincides with the vortex center and the radius is equal to the distance from the center to the nearest surface of the disk. For a solid disk and an annular disk at $\eta = 0.1$, there are no obvious ICRVPs, i.e., $\Gamma'_i = 0$. For disks with larger central holes, Γ_i decreases as long as $\eta > 0.3$. On the other hand, the outer vortex continues increasing with higher η, which causes the absolute value of $\Gamma' = ||\Gamma_i| - |\Gamma_o||$ to gradually decrease, proving that in Figs. 8(k)–8(o) the relative intensity of the OCRVP and ICRVP tends to accord. For the time evolution of the vortex pairs in Fig. 9(b), the absolute values of Γ_o are observed to increase
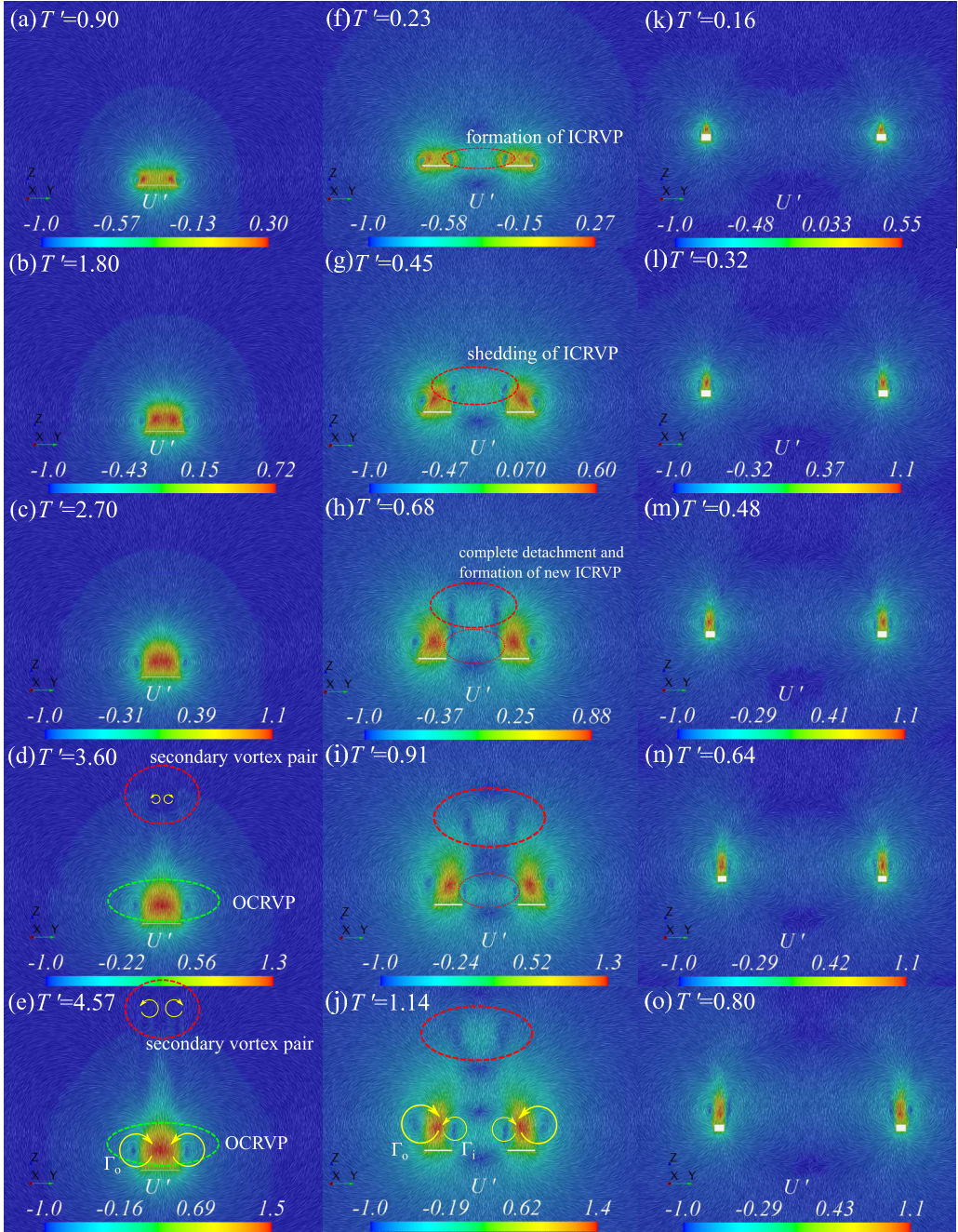
FIG. 8. LIC maps at different moments before the onset of the wake instability at $\eta = 0, 0.5$, and 0.9. The nondimensionalized time is defined as $T' = t/(D/|\bar{U}_z|)$, where t is the physical falling time, D is the outer diameter, and $\bar{U}_z$ is the mean vertical falling velocity. A secondary vortex pair is induced by the OCRVP for the solid disk from (a) to (d). Both the inner and outer edges can generate counter-rotating vortex pairs, but the inner edges shed from the surface constantly at moderate $\eta = 0.5$ from (f) to (j). For the flat ring at $\eta = 0.9$ from (k) to (o), the ICRVP is elongated gradually since $T' = 0.64$, and the unstable interaction between the vortex pairs leads to path instability.
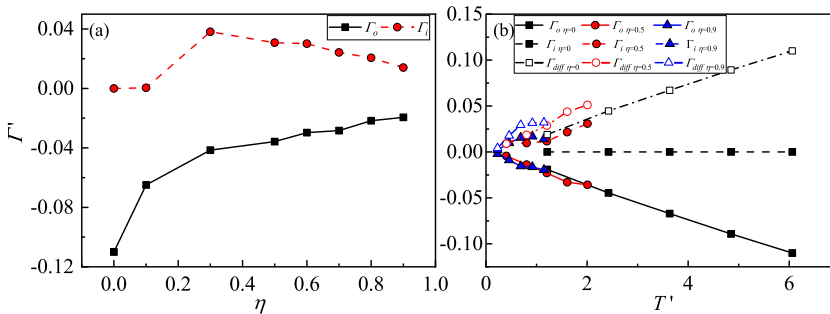
FIG. 9. (a) The velocity circulation varying with η and (b) the time evolution of vortex circulation at $\eta = 0$, 0.5, and 0.9 before the onset of the wake instability. The velocity circulation is nondimensionalized as $\Gamma' = \Gamma / D\sqrt{gD}$. The anticlockwise and clockwise vortices are defined as negative and positive circulations, respectively.

throughout the whole time before symmetry is lost, while the solid disk can sustain the longest stable status. The equivalent vorticity $\Gamma_{\text{diff}} = |\Gamma_o| - \eta\Gamma_i$ [depicted in Fig. 9(b) as open symbols] is calculated to measure the "lever arm" effect as suggested by Vincent *et al.* [33]. Γ_{diff} at $\eta = 0$ and $\eta = 0.5$ increases linearly with time, while Γ_{diff} at $\eta = 0.9$ approaches a constant value near 0.032, indicating that the ICRVP and OCRVP tend to be stable after the falling is well established. Vincent *et al.* [33] found that the presence of the inner vortex ring decreases the overall circulation and stabilizes the falling. However, this stabilization mechanism is attenuated for the high η and relatively low Re conditions where the annular disks exhibit more irregular motion due to the smaller intensity of ICRVP and OCRVP compared to the disk inertia. And neither the ICRVP nor OCRVP can dominate in determining the relative attitude of the disk.

B. Dimensionless moment of inertia I^*

The moment of inertia describes the magnitude of the inertia of the disk for its rotational movement, and the rotation motion around the z axis in the body-fixed coordinate system determines the fluid torque acting on the disk. However, previous studies have mainly focused on a constant dimensionless moment of inertia I^*. In this section, the inner to outer diameter ratio η and density ratio ρ^* are kept at 0.4 and 1.2, respectively, and we focus on the influence of different I^* on the disk rotation characteristics and the falling trajectory. Different from previous studies, the dimensionless moment of inertia I^* explored in this work is limited within a small range to prevent the potential tumbling motion (generally speaking, $I^* < 10^{-2}$ can be considered a "small" dimensionless moment of inertia [13]), as listed in Table V. The corresponding Reynolds number Re_{U_z} fluctuates between 616 and 673, which indicates that the turbulent mode does not change dramatically within the range.

First, the horizontal trajectories under different I^* are depicted in Fig. 10, showing a full development of the 3D trajectory for each disk. Similar to other falling motions, the disk undergoes a short-term planar oscillation after being released from still and then develops into a 3D motion

TABLE V. The dimensionless moment of inertia I^* and the corresponding Reynolds number Re_{U_z}. η and ρ^* are kept at 0.4 and 1.2, respectively. Re_{U_z} has little effect on the flow pattern owing to the narrow range from 616 to 673.

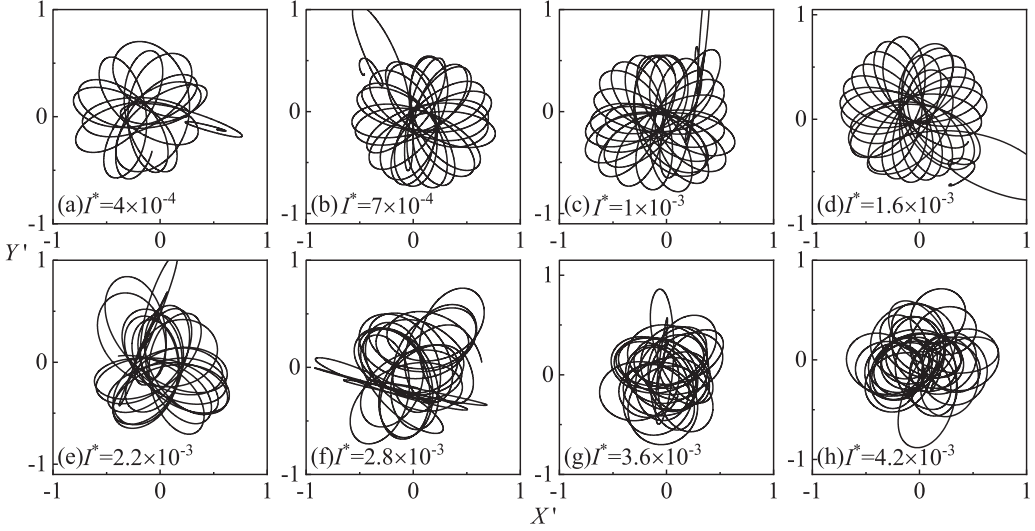| I^* ($\times 10^{-4}$)	4	7	10	16	22	28	36	42
Re_{U_z}	673	649	634	616	623	617	631	644

FIG. 10. Horizontal trajectories of the disks at different I^*. With the increment of I^*, each period of the planar trajectories tends to be a more irregular ellipse. See also Video S4 of the Supplemental Material [45] for the disk at $I^* = 7 \times 10^{-4}$.

in space. At $I^* \leqslant 1.6 \times 10^{-3}$, the horizontal trajectories of the disk present the characteristics of a typical HH motion with a relatively regular oblate petal-like shape and an approximately equal amplitude of precession. With a higher I^* than 1.6×10^{-3}, the repeatability of each period diminishes, and the center of the horizontal orbit is inconsistent. Although the trajectories still maintain the basic HH motions, the precession frequency seems much more irregular.

To quantitatively describe the characteristics of the horizontal trajectories, Fig. 11 shows the mean displacement and velocity amplitude of the planar trajectories, as well as the fluctuation range of the precession motion. For the conventional HH motion at $I^* \leqslant 1.6 \times 10^{-3}$, the mean amplitude of displacement increases slowly with a wider distribution area of the trajectory. However, with a further increment of I^*, the petal-like orbit of each period becomes circular as the trajectories are concentrated around the original falling point. Since the motion of the disk is a fully developed 3D curve around the vertical axis in space, the mean velocity is slowed down, and the fluctuation range is also decreased due to the larger resistance against the angular motion caused by the larger I^*.
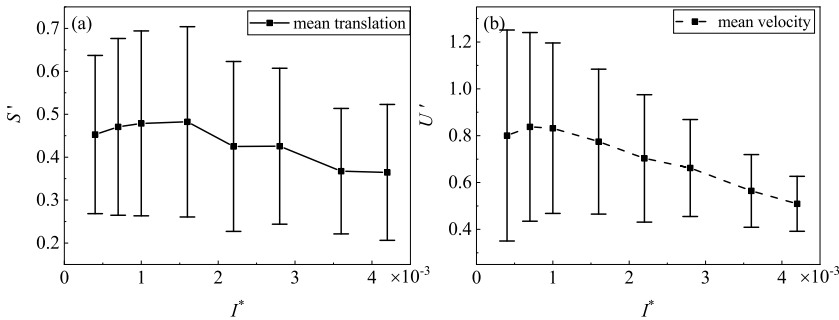

FIG. 11. (a) Horizontal translations and (b) velocity fluctuations of the disks at different I^*. The mean horizontal velocity is slowed down by the higher I^* along with smaller fluctuations.
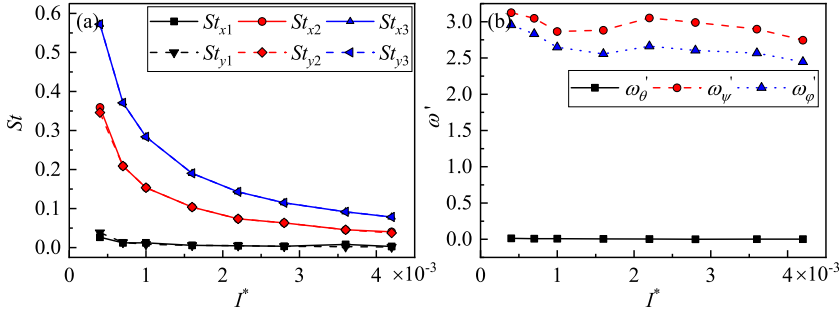
FIG. 12. (a) The Strouhal number St of the horizontal trajectories of the disks at different I^*. (b) The mean angular velocities of the disks at different I^*.

The disks wobbling around the center of the trajectories may exhibit different frequencies, which have received little attention in previous studies. In Fig. 12(a), we focus on the oscillating behaviors represented by the Strouhal number St where the frequency is determined using a fast Fourier transform. Three dominating Strouhal numbers in the x and y directions, namely, St_1, St_2, and St_3, have been identified for the horizontal trajectories, where St_1 and St_2 stand for the oscillation of the major and minor axes of the semielliptical orbit, respectively, and St_3 is a type of long-periodic movement. An exponential decline in St_1 and St_2 is observed with an increment of I^*, while the long-period oscillation maintains a relatively small value. It is worth noting that St_1 is approximately two times that of St_2, which can be demonstrated in Fig. 13, where an enlarged diagram of only several periods of the horizontal paths from positions A to E shows that the major axis changes its direction twice compared to the minor axis. Since I^* mainly characterizes the disk's ability to resist rotating movement, Fig. 12(b) presents the mean angular motion of the disk during the falling process. The overall picture for the precession angular velocity ω'_ψ and the rotation angular velocity ω'_ϕ is that a small bump occurs near $I^* = 2.2 \times 10^{-4}$ where the trajectories begin to irregularly precess. The nutation angle θ describes the angle between the z' axis of the disk and the world coordinate system Z axis, while for all the conditions investigated, the nutation angle θ is nearly zero. In general, a larger I^* means more damping effects on the disk to attenuate the fluid forces.
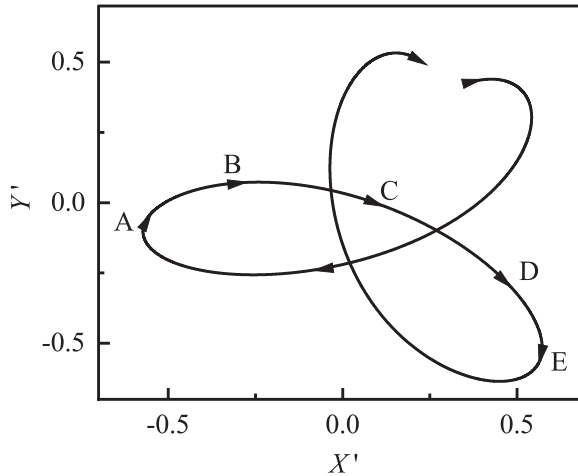

FIG. 13. The horizontal trajectory in three periods of the disk for $I^* = 7 \times 10^{-4}$. A through E denote the five positions in one period.
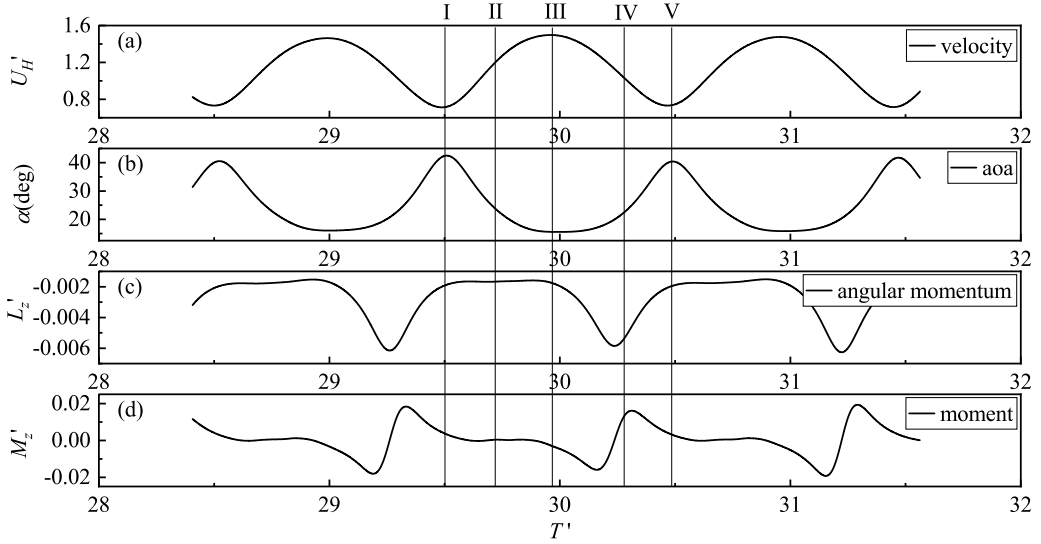
FIG. 14. The time evolution of the kinematic and dynamic quantities, namely, the (a) horizontal velocity U_H', (b) angle of attack α, (c) angular momentum L_z', and (d) fluid moment M_z' about the z axis of the disk for $I^* = 7 \times 10^{-4}$. I–V are the corresponding instantaneous times referring to A–E in Fig. 13 and Figs. 15(a)–15(e).

The correlation describing variations of the trajectory with flow structures and the dynamic characteristics is further explored in Figs. 13–15, where one period at $I^* = 7 \times 10^{-4}$ is analyzed from positions A to E with respect to the kinematic and dynamic characteristics at different instantaneous times from I to V and its vortical structures from (a) to (e). Considering the extreme points A, C, and E in Fig. 13 and the mean horizontal velocity U_H' and angle of attack α at I, III, and V in Fig. 14, it can be seen that the extrema of the trajectory are consistent with the kinematic features. However, at position A with the largest horizontal displacement, the angular momentum L_z' and fluid moment M_z' slowly reach a small and flat stage, which leads to the disk gliding almost linearly between positions B and C. In Fig. 15(a), the counter-rotating vortex pair (CRVP) resembling the wing-tip vortices is generated by the outer edge, which can balance the inertial motion of the disk. However, as the angle of attack decreases, one pole of the tip vortices
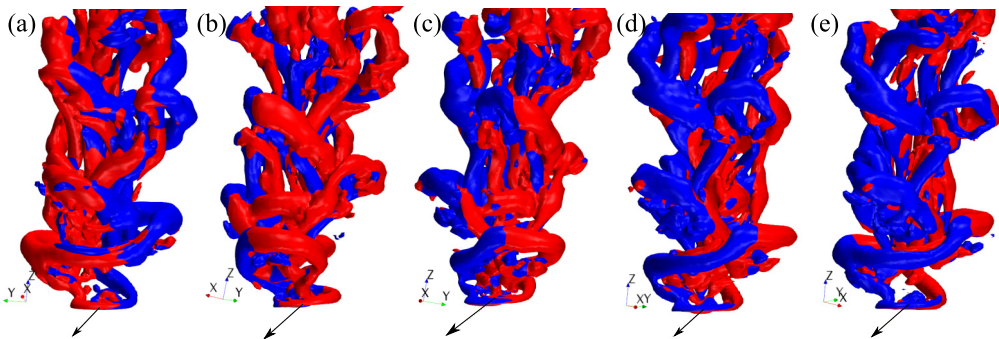

FIG. 15. The time sequence of flow structures behind the disk at different times for $I^* = 7 \times 10^{-4}$. (a)–(e) Corresponding instantaneous vortical structures at positions A–E in Fig. 13; the arrows indicate the velocity vectors at the positions.

TABLE VI. Density ratio ρ^* and corresponding Reynolds number Re_{U_z}. Similar to the relation between I^* and Re_{U_z} in Sec. III B, Re_{U_z} can be deemed to have negligible effects on the flow pattern because of the narrow range from 597 to 622.

ρ^*	1.2	2	3	4	5	6
Re_{U_z}	622	608	602	600	597	600

on the concave side of the horizontal trajectory diminishes gradually and detaches finally from the disk, during which the vortex formed by the inner edge moves toward the center of the hole and soon sheds completely from the disk, as shown in Figs. 15(b) and 15(c). After position C, the absolute value of the external fluid forces and torque starts to increase slowly with an opposite direction, while due to the lag of the inertia the disk is still gliding until position D. Throughout the whole period of the planar motion, it can be found that one pole of the vortex pair on the convex side is continually generated by the outer edge, but the other pole on the concave side sheds periodically from the disk, which can yield periodic oscillating fluid forces and torques on the disk.

C. Body to fluid density ratio ρ^*

For a specific fluid, the body to fluid density ratio ρ^* is another key factor that affects the free fall of the disk. To analyze the trajectory and flow field characteristics of the annular disks at different ρ^*, we keep a constant dimensionless moment of inertia at $I^* = 7 \times 10^{-4}$ and a moderate inner and outer diameter ratio $\eta = 0.4$ and gradually increase the body to fluid density ratio ρ^* from 1.2 for a lighter disk to 6 for the heaviest disk. It is obvious that ρ^* must be larger than 1 to ensure a free-fall movement; on the other hand, to increase ρ^* while keeping other parameters such as I^* and η invariable and to reach a reasonable geometrical size, $\rho^* = 6$ is the maximum value that we can obtain. The Reynolds number Re_{U_z} changes from 597 to 622 within a narrow range, as shown in Table VI.

As with the same analysis as in the previous sections, first, the horizontal trajectories are compared under the conditions of different ρ^*, as shown in Fig. 16. The falling style sustains the classic HH motion for the whole range of ρ^* after a short transitional state in the initial release. However, it seems that for the lighter disks, it takes longer time to settle into a stable precession state, as more irregular periods can be seen after being released from still for $\rho^* = 1.2$ and $\rho^* = 2$.

Similarly, the amplitude S' and mean velocity U'_H of the horizontal movement of the disk also increase slightly within the range of ρ^*, as shown in Fig. 17(a). The oscillation amplitude exhibits an identical trend. Compared to Fig. 12(a), where three Strouhal numbers are recognized and St_3 represents the long-period oscillation for the "nonstandard" HH motion, this third Strouhal number cannot be observed for the standard HH motion from lightest to the heaviest disks in Fig. 17(b), while St_2 is still approximately two times more than St_1. A larger ρ^* plays a similar role as I^* in enhancing the disk inertia effect to resist the fluid force acting on the disk's surface.

Although ρ^* has little effect on the motion styles of the disk, the fluid force on the disk changes significantly with the density ratio, as shown in Fig. 18, where the vertical fluid force $\mathbf{F_{ver}} = \mathbf{F}_\omega - \mathbf{F_n}$ provides the counterbalance force against gravity, $\mathbf{F}_\omega$ is the total fluid force, and $\mathbf{F_n}$ is the normal force providing the centrifugal force to make the petal-like horizontal path. In short, the force analysis decomposes the total fluid force into the vertical and horizontal directions, which are our primary concerns about the characteristics of the falling trajectory. For all the fluid forces, rapid growth can be found due to the increment of the inertial mass. It is worthwhile to note that the larger variance of the fluid forces can lead to a wider unsteady motion range. Since all the disks exhibit a normal HH motion characterized by a petal-like horizontal trajectory, the mean amplitude F_n grows linearly with ρ^*. However, a dispersion degree of F_n is also observed to increase because a much higher F_n is exerted near the vertex of the horizontal trajectory.
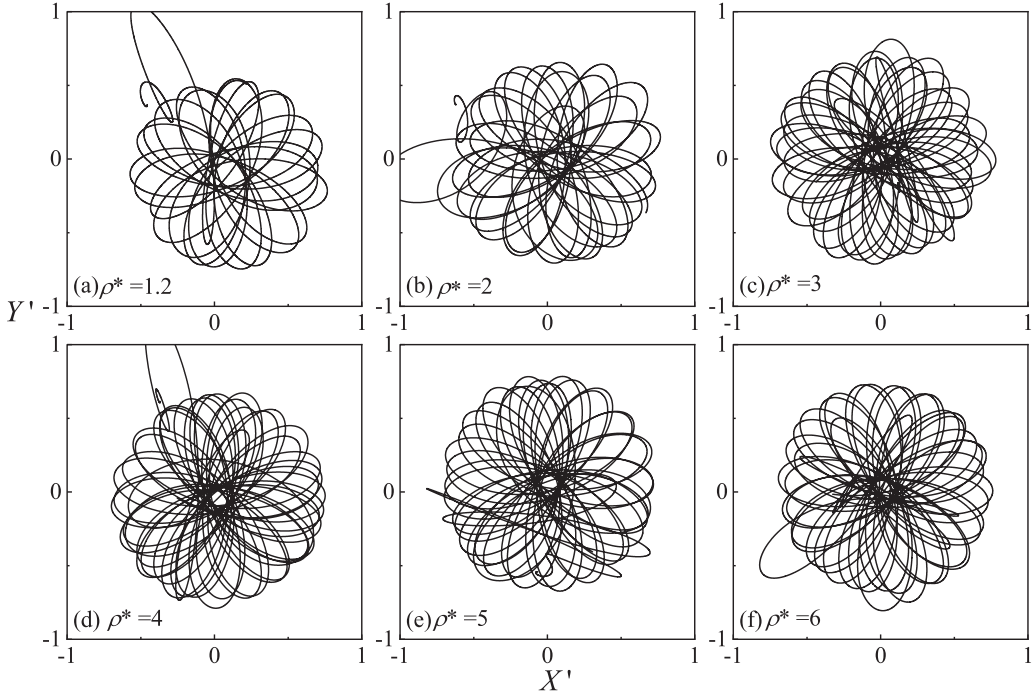
FIG. 16. The horizontal trajectories of the disks at different ρ^*. For the whole range of ρ^* considered, only the typical HH motions are observed after the falling process has been fully established.

Figure 19 shows the instantaneous wake structures of the disks at different ρ^* after the flow has been fully developed. Due to its regular HH motion, no prominent disparities can be found compared to Fig. 15, where vortices are generated and detached at both the inner and outer edges. However, as ρ^* increases, the area surrounded by continuous outer vortices contains more streamwise vortices that are induced by the flow passing through the central hole. More discrete small-scale vortices are induced by the growing intensity of the outside vortices, and the dispersion of the central streamwise vortices becomes larger in a wider area.

A significant vortical structure of the annular disk we observed is the complex streamwise vortices encircled by the twisted outside vortices. To analyze this special flow characteristic, Fig. 20
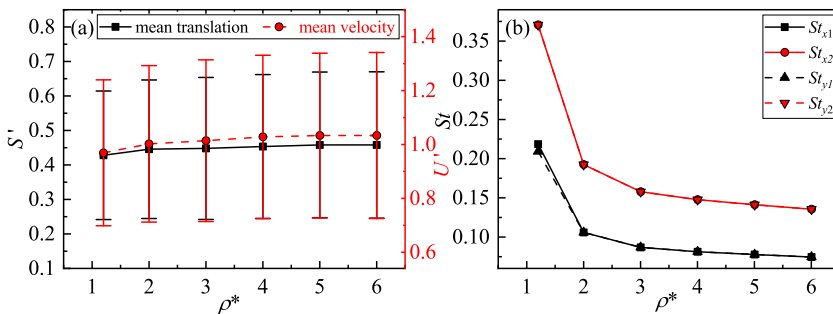

FIG. 17. (a) Amplitude and mean velocity. (b) Strouhal numbers of horizontal trajectories at different ρ^* values from 1.2 to 6. The trajectories are slightly influenced by ρ^*, but St decreases dramatically with increasing ρ^*.
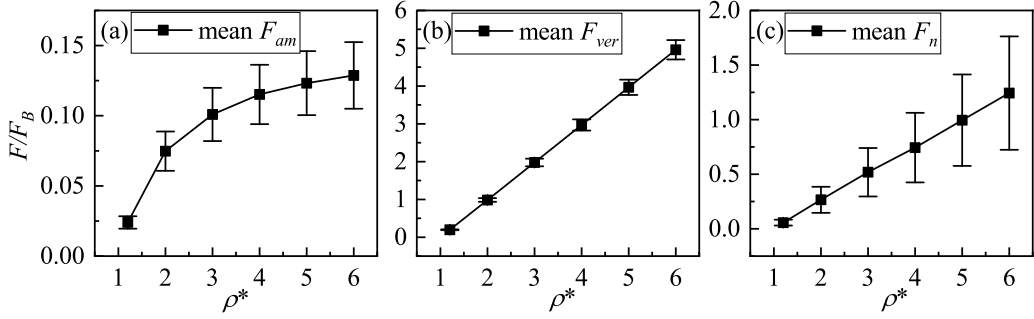
FIG. 18. The mean and variance of (a) added-mass force $\mathbf{F_{am}}$, (b) vertical fluid force $\mathbf{F_{ver}}$, and (c) centrifugal force $\mathbf{F_n}$ acting on the disks at different ρ^*.

presents a partially enlarged view of the instantaneous wake structure near the upper surface of the disk at $\rho^* = 2$. We take the stagnation point P_S against the incoming flow on the outer rim of the disk. At an instantaneous moment, the disk's movement is the superposition of the translational velocity of the center of mass, $\mathbf{V_c}$, and the tangential velocity $\mathbf{V_r}$, where $\mathbf{V_r} = \omega_\phi \times \mathbf{R}$, with $\mathbf{R}$ being the direction vector from the center of mass to stagnation point P_S and ω_ϕ the angular velocity around the axis of rotation z' in the body-fixed coordinate. Starting from the stagnation point P_S, the
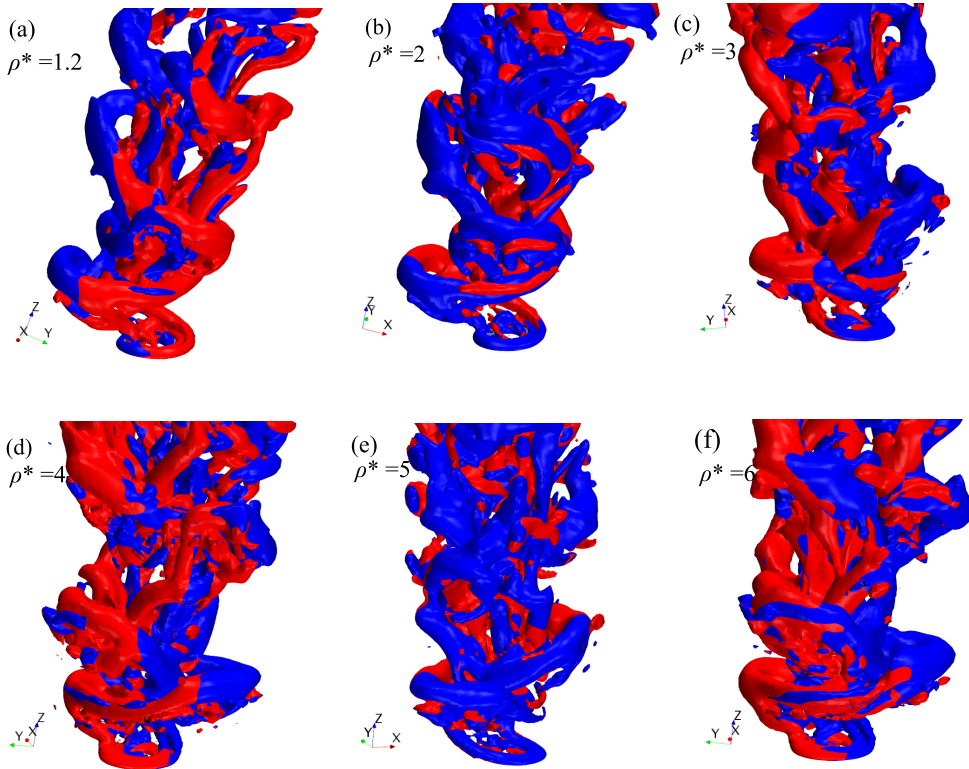

FIG. 19. The instantaneous vortical distributions of the disk at different ρ^*. The color code is the same as in Fig. 7.
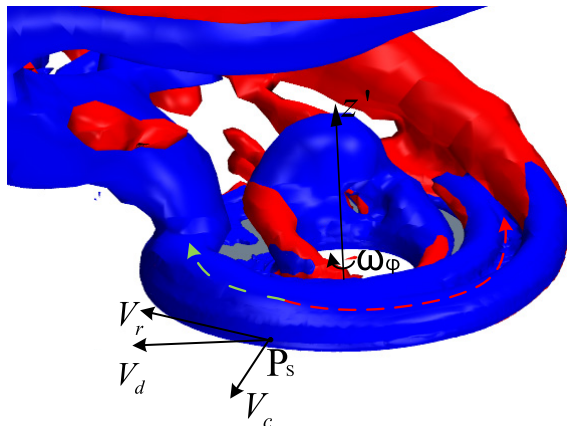
FIG. 20. Detailed vortical structures near the surface of the disk at $\rho^* = 2$.

fluid flows toward both sides, as shown by the green and red dashed lines. The green dashed line points to the inner side of the trajectory where the fluid accumulates gradually until detaching from the surface of the disk. The red dashed line is the direction of flow separation where the fluid flows on the surface for a relatively long distance and separates from the outer vortex but still attaches to the surface. A new kind of triangular vortical structure is generated by the inner rim of the disk. With the process of accumulation progressing inside of the trajectory, the vortex will contact and merge with the triangular vortex, and the composite vortex structures finally shed from the disk and turn into the central streamwise vortex.

D. The mechanism of planar precession

HH motion has been widely encountered in a large range of the parameter space for both solid [16] and annular disks [34] since it was first defined by Auguste *et al.* [18]. The horizontal trajectory of each period of HH motion is a petal-like or semielliptical curve, where the major axis of the ellipse keeps precessing over time around the vertical direction, similar to the apsidal precession of a celestial body's orbit in astronomy. However, the mechanism of planar precession is not fully understood. Therefore, in this section, we attempt to demonstrate the deep reason for the precession of an annular disk at typical parameters of $I^* = 7 \times 10^{-4}$, $\eta = 0.4$, and $\rho^* = 1.2$ by a comprehensive analysis of the temporal evolution of trajectory, fluid forces, and vortical structures.

Figure 21 shows several periods of the horizontal trajectories, where the yellow arrows point in the direction of normal force F_n and A through F are the corresponding extrema of F_n, L denotes the vertex of the semielliptical path, and S' and α are the mean displacement and angle of attack, respectively. A small gap between the peak values of F_n at point A and vertex L of the horizontal path can be observed in Fig. 21, which means that hysteresis occurs in the disk's kinematic and dynamic characteristics, but the phase difference of the three curves remains constant throughout the whole falling process. Namkoong *et al.* [47] reported a similar phenomenon in the study of the free motion of a two-dimensional cylinder. The lift disappeared when the vortex shed, and then the displacement of the cylinder reached its maximum point, where the same phase difference appeared between the falling trajectory and fluid force evolution.

The correlation between the vortical structures and fluid force reveals more details, as depicted in Fig. 22. At moment A, the disk approaches the extreme point of the trajectory with the largest angle of attack, producing a high drag force to decelerate. A triangular vortex is formed at the rear of the inner edge, and the two poles of the CRVP at the outer edge with nearly equal intensity still attach to the disk, leading to a minimum F_n. From B to C, due to the accumulation effect at the stagnation point as described in the previous section, the inner pole of the CRVP detaches from the
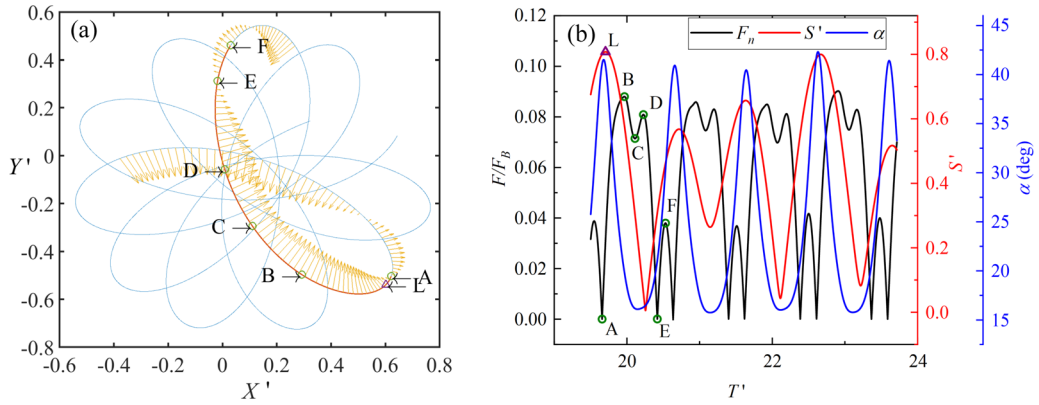
FIG. 21. (a) The planar trajectory; (b) the magnitude of normal force F_n, mean displacement S', and angle of attack, α. The yellow arrow in (a) is the instantaneous direction of F_n. A through F are the extreme points (local minimum or maximum point) of F_n, and L is the vertex of the semielliptical path. See Video S5 of the Supplemental Material [45] for the dynamic behavior of the disk at $I^* = 7 \times 10^{-4}$, $\eta = 0.4$, and $\rho^* = 1.2$.
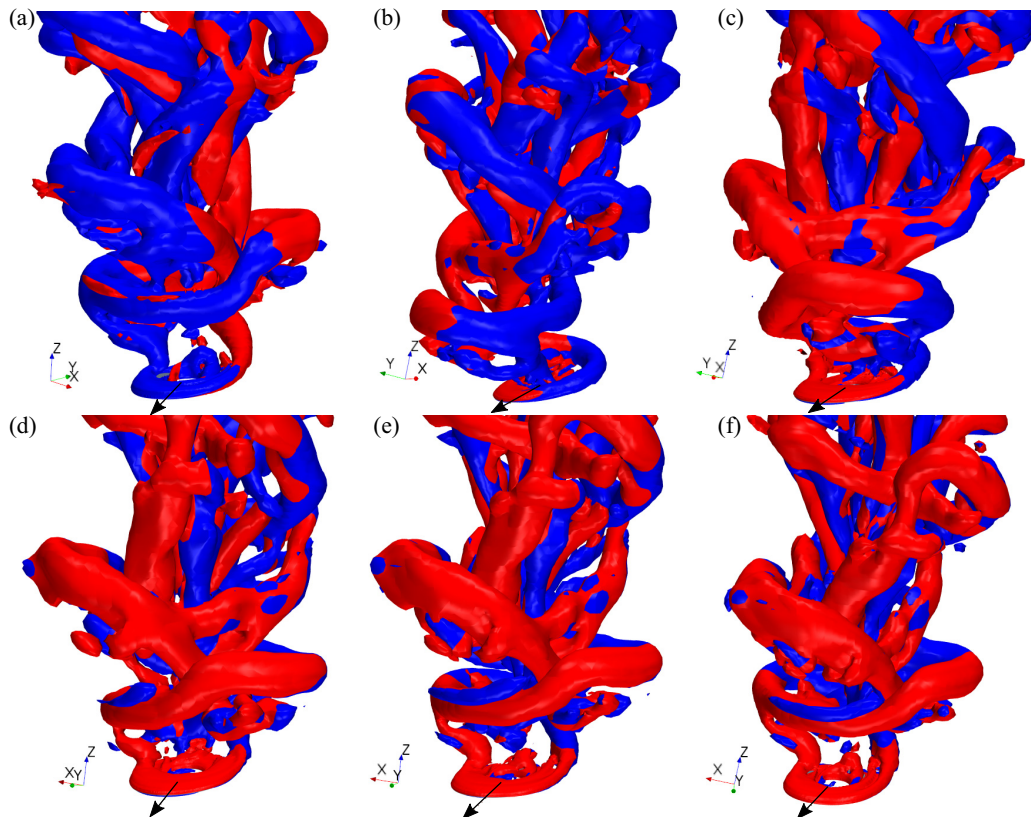

FIG. 22. The vortical structures of the disk at different moments corresponding to A through F in Fig. 21. The arrow is indicative of the velocity direction.
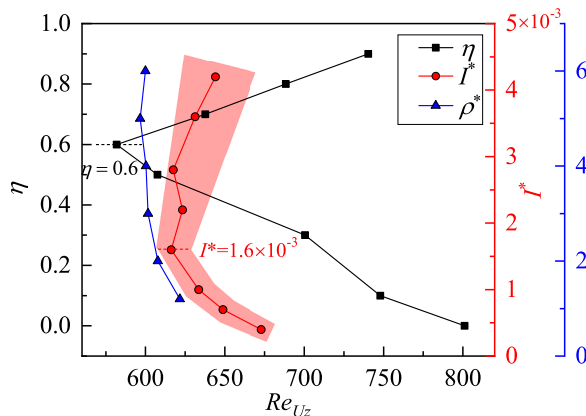
FIG. 23. The parameter regime of disks. The color code of the line is consistent with the y axis. The black dashed line is indicative of the threshold for the change of falling motions from HH motion to LI motion at $\eta = 0.6$. The red shadow denotes that the falling remains HH motion while slightly changing its pattern near the red dashed line at $I^* = 1.6 \times 10^{-3}$. In the whole range of ρ^*, the falling pattern is typical HH motion.

disk and merges with the triangular structure. Then, the vortex is driven by the fluid passing through the central hole to move downstream and gradually elongates to form streamwise vortices. From B to D, the disk glides along a curve with relatively large curvature and a small angle of attack, α, during which the vortex in the inside begins growing. Within the whole process, a continuous vortex is formed at the outer edge in the outside direction of the trajectory, which exerts a persistent force on the disk. Point E is similar to point A with an equal intensity of CRVP on both sides of the disk. However, it should be noted that Fig. 21(b) gives the absolute value of F_n, while in fact, as shown in Fig. 21(a), F_n alters its direction at points A and E. Different from the regular circular planar path, it is the unsteady normal force F_n in each period providing the centrifugal force that causes the precession of the plane trajectory, and F_n is closely related to the generation and detachment of the vortices.

IV. DISCUSSION AND CONCLUDING REMARKS

In the current work, based on the well-established numerical method, we presented a comprehensive investigation of the influencing factors on the free fall of annular disks. By combining the kinetic and dynamic characteristics, three primary dimensionless parameters are taken into account: the inner and outer diameter ratio η, the dimensionless moment of inertia I^*, and the body to fluid density ratio ρ^*. The correlations among the vortical structures, fluid forces, and falling trajectories are discussed in detail. Figure 23 presents a regime map of the disks in this work, where all the geometric parameters, η, I^*, and ρ^*, are designed to cover a wide range in the parameter space while maintaining practicable sizes, i.e., neither too small nor too large. The Reynolds numbers considered in the current study are approximately from 550 to 800 to eliminate the effect of flow transition. However, detailed transition scenarios are still required in future studies.

The inner and outer diameter ratio η has a major impact on the falling trajectory as well as the flow structures. The annular disks pass through a sequence of regular HH motion and LI motion from $\eta = 0$ for a solid disk to $\eta = 0.9$ for a flat ring, which is different from the previous study in which the central hole can stabilize the falling process. Since η varies dramatically from 0 to 0.9, as shown in the regime map of Fig. 23, Re_{Uz} gradually decreases in the range of $\eta = 0$–0.6 and increases approximately linearly after $\eta = 0.6$. The characteristics of the mean angle of attack and mean fluid forces acting on the disk also support that $\eta = 0.6$ is a turning point for different falling types. LI motion exhibits a much larger transverse displacement in the horizontal plane compared to

the common "regime A" [13], and more discrete vortices can be found in the wake. Both the inner and outer edges can generate a larger-scale CRVP, but the inner vortices periodically shed from the disk, which finally makes the disk tilt to another side. For the disk of high porosity, the strength of CRVPs tends to equalize, and none of the vortices can be dominant in the near wake of the disk, which leads to a more unstable interaction. The time evolution of the velocity circulation of the CRVP can also support that the relative intensity between the inner and outer vortices decreases for higher η.

It has been shown that the dimensionless moment of inertia I^* has fewer effects than η since all the disks exhibit HH motion within the scope of the parameters considered in this work. However, as I^* increases, the trajectories in the horizontal plane gradually become irregular, but each period still maintains a petal-like form. In Fig. 23, Re_{U_z} weakly increases after $I^* = 1.6 \times 10^{-3}$ compared to the sudden change of $\eta - \mathrm{Re}_{U_z}$, where the repeatability of each period diminishes. Since I^* mainly affects the rotating characteristics of the disk, it can be seen that the overall picture of the precession angular velocity ω'_ψ and the rotation angular velocity ω'_ϕ decreases with the increment of I^*, meaning that the higher I^* disks can provide more resistance against the flow. Then, an analysis on a disk of $I^* = 7.0 \times 10^{-4}$ reveals that the disk's dynamic parameters, such as angular momentum and fluid moment, have a close correlation with the vortical structures.

Contrary to the intuitive understanding, the body to fluid density ratio ρ^* has a negligible effect on the kinematic characteristics of the disk within the parameters considered, in which regular HH motion is maintained, as shown in Fig. 23 where Re_{U_z} exhibits a slow decrement within a narrow range from 622 to 597. However, to resist the increment of the inertial force of the disk with higher ρ^*, the fluid forces exerted on the disk gradually increase, but the oscillation range becomes broader. In the case of high ρ^*, more discrete vortices are induced by the large-scale vortical structures. A special flow state near the upper surface of the disk is found to be important for the formation and development of different vortical structures on the inner and outer sides of the disk. Furthermore, we have demonstrated the primary reason for the precessional planar path of the most common HH motion by a comprehensive analysis of the kinematic and dynamic characteristics as well as the flow structures. A hysteresis effect is observed between the horizontal displacement and the fluid forces, which is caused by the periodic movement of the inner pole of the CRVP.

The previous investigations on the freely falling bodies mainly focused on the fundamental fluid-structure interactions between the bodies and the surrounding fluids in the area of mechanics and bionics. With the development of MEMS, a wind-dispersed passive microflier carrying wireless electronic chips can be manufactured for various applications [8,36]. Considering the parameter regime of the disks in Fig. 23 again, it can provide potential guidance on the design of annular passive microfliers through an elaborate parameter selection as a stabilization strategy to realize longer traveling distance, predictable landing site, and lower terminal velocity. By revealing the coupling interaction between the disk's pose and wake structures, this work can further shed light on the control mechanism of the passive microfliers.

APPENDIX

To separate the added-mass force from the total hydrodynamic force, first, the added-mass coefficient has to be determined. Previous studies have investigated the added-mass coefficients of homogeneous objects such as spheres, cubes, and solid disks, mainly including the boundary element method [48], slender body theory [49], and potential flow theory [50]. In this paper, referring to research by Sherwood and Stone [50] and Sherwood [51] on the added-mass force of a

solid disk, the current method is based on the potential flow theory to deduce the law of added-mass coefficient against the change of the inner to outer diameter ratio η.

The incompressible Euler equation for an ideal fluid is

$$\frac{\partial \mathbf{u}}{\partial t} + (\mathbf{u} \cdot \nabla)\mathbf{u} = -\frac{1}{p}\nabla p + \mathbf{g}, \tag{A1}$$

where $\mathbf{g}$ is the gravity force and the only body force in the field.

Based on the vector identities,

$$\mathbf{u} \times (\nabla \times \mathbf{u}) = \nabla\left(\frac{\mathbf{u} \cdot \mathbf{u}}{2}\right) - (\mathbf{u} \cdot \nabla)\mathbf{u}. \tag{A2}$$

The Euler equation can be written as

$$\frac{\partial \mathbf{u}}{\partial t} + \nabla\left(\frac{u^2}{2}\right) - \mathbf{u} \times \mathbf{\Omega} = -\frac{1}{p}\nabla p + \mathbf{g}, \tag{A3}$$

where $\mathbf{\Omega}$ is the curl of the velocity vector, $\mathbf{\Omega} = \nabla \times \mathbf{u}$.

Suppose the disk is moving along its axis of rotation, and we can obtain the velocity potential

$$\phi(\mathbf{x}) = \mathbf{U}(t)\Phi(\mathbf{x} - \mathbf{x}_0(t)), \tag{A4}$$

where $\mathbf{U}(t)$ is the velocity vector of the center of mass, Φ is the velocity potential near the disk, $\mathbf{x}_0$ is the instantaneous position of the center of the disk, and $d\mathbf{x}_0/dt = \mathbf{U}$.

Because of the hypothetical irrotational and inviscid flow, i.e., $\mathbf{\Omega} = \nabla \times \mathbf{u} = 0$, Eq. (A3) can be written as

$$\nabla\left(\frac{\partial \phi}{\partial t} + \frac{1}{2}u^2 + \frac{p}{\rho} - \mathbf{g}\right) = 0. \tag{A5}$$

Integrate Eq. (A5) and we can obtain

$$\frac{\partial \phi}{\partial t} + \frac{1}{2}u^2 + \frac{p}{\rho} - \mathbf{g} = C, \tag{A6}$$

where C is a constant.

The fluid force can integrate the pressure over the solid disk surface:

$$\mathbf{F} = -\int_S p\mathbf{n}dA. \tag{A7}$$

Substituting Eq. (A6) into Eq. (A7),

$$\mathbf{F} = \rho\int_S \frac{\partial \phi}{\partial t}\mathbf{n}dA + \frac{1}{2}\rho\int_S \mathbf{u}^2\mathbf{n}dA - \rho\int_S \mathbf{g} \cdot \mathbf{x}\mathbf{n}dA. \tag{A8}$$

The third term of the right-hand side of Eq. (A8) equals zero. For the first term of the right-hand side,

$$\frac{\partial \phi}{\partial t} = \dot{\mathbf{U}} \cdot \Phi + \frac{\partial(\mathbf{x} - \mathbf{x_0})}{\partial t} \cdot \nabla\phi = \dot{\mathbf{U}} \cdot \Phi - \mathbf{U} \cdot \mathbf{u}. \tag{A9}$$

Substituting Eq. (A9) into Eq. (A8), the fluid force becomes

$$\mathbf{F} = \rho\dot{\mathbf{U}} \cdot \int_S \Phi\mathbf{n}dS + \rho\int_S\left[\frac{1}{2}u^2 - (\mathbf{U}\nabla)\phi(\mathbf{x} - \mathbf{x_0})\right]\mathbf{n}dS. \tag{A10}$$

In Eq. (A10), the second term on the right-hand side is caused by the body's steady motion $\dot{\mathbf{U}}$, while the first term is the added-mass force due to unsteady motion, $\mathbf{G} = -C_{am}\rho_f\dot{\mathbf{U}}$.

For a disk moving in an infinite region of fluid, the velocity potential has been well developed in oblate spheroidal coordinates [50–52]:

$$\Phi(r, z) = \frac{2}{\pi}[z\cot^{-1}(\lambda) - \zeta] \qquad (0 \leqslant \zeta \leqslant 1, 0 \leqslant \lambda < \infty), \tag{A11}$$

where (r, z) are the cylindrical coordinates with origin in the center of the disk, radial coordinate r, and axial coordinate z aligned with the rotation axis of the disk. The oblate spheroidal coordinates (λ, ζ) are defined as

$$z = \lambda\zeta, \quad r^2 = (1 + \lambda^2)(1 - \zeta^2). \tag{A12}$$

Here, $\lambda = 0$, $0 \leqslant \zeta \leqslant 1$, which represents the surface of the disk. Then, we can obtain $\Phi(r, z) = -2/\pi\sqrt{1 - r^2}$ by substituting λ and ζ into Eq. (A11). From Eq. (A10) the acceleration reaction on the body becomes

$$C_{am} = -\frac{\mathbf{G}}{\rho\dot{\mathbf{U}}} = -\frac{2}{\pi}2\int_{\eta}^{1}(1 - r^2)^{1/2}2\pi\,dr = \frac{8}{3}(1 - \eta^2)^{3/2}, \tag{A13}$$

where η is the inner to outer diameter ratio.

The authors would like to address that the derivation above of the added-mass coefficient is based on an ideal inviscid fluid, and it is also assumed that the disk is moving along the axis of symmetry. The added-mass coefficient is only related to the shape of the object, and for a specific object, the added-mass force coefficient is a constant value. Since we focus on the influence of the force generated by the vortex motion due to movement of the disk, the estimation of the added-mass force does not affect the general discussions [53,54].

---

[1] I. Newton, *The Principia: Mathematical Principles of Natural Philosophy*, Vol. 2, translated by I. B. Cohen and A. Whitman (University of California Press, Oakland, CA, 1999), first published 1687 in Latin.

[2] V. Mathai, X. Zhu, C. Sun, and D. Lohse, Mass and Moment of Inertia Govern the Transition in the Dynamics and Wakes of Freely Rising and Falling Cylinders, Phys. Rev. Lett. **119**, 054501 (2017).

[3] R. Norberg, Autorotation, self-stability, and structure of single-winged fruits and seeds (samaras) with comparative remarks on animal flight, Biol. Rev. **48**, 561 (1973).

[4] G. Mougin and J. Magnaudet, Path Instability of a Rising Bubble, Phys. Rev. Lett. **88**, 014502 (2001).

[5] R. Zenit and J. Magnaudet, Path instability of rising spheroidal air bubbles: A shape-controlled process, Phys. Fluids **20**, 061702 (2008).

[6] P. Kry and R. List, Angular motions of freely falling spheroidal hailstone models, Phys. Fluids **17**, 1093 (1974).

[7] C. Cummins, M. Seale, A. Macente, D. Certini, E. Mastropaolo, I. M. Viola, and N. Nakayama, A separated vortex ring underlies the flight of the dandelion, Nature (London) **562**, 414 (2018).

[8] B. H. Kim, K. Li, J.-T. Kim, Y. Park, H. Jang, X. Wang, Z. Xie, S. M. Won, H.-J. Yoon, G. Lee *et al.*, Three-dimensional electronic microfliers inspired by wind-dispersed seeds, Nature (London) **597**, 503 (2021).

[9] H. Viets and D. Lee, Motion of freely falling spheres at moderate Reynolds numbers, AIAA J. **9**, 2038 (1971).

[10] G. Stringham, D. B. Simons, and H. P. Guy, *The Behavior of Large Particles Falling in Quiescent Liquids* (U.S. Government Printing Office, Washington, DC, 1969).

[11] T. Yaginuma and H. Itō, Drag and wakes of freely falling 60° cones at intermediate Reynolds numbers, Phys. Fluids **20**, 117102 (2008).

[12] W. Wang, R. Hu, S. Xu, and Z. Wu, Influence of aspect ratio on tumbling plates, J. Fluid Mech. **733**, 650 (2013).

[13] P. Ern, F. Risso, D. Fabre, and J. Magnaudet, Wake-induced oscillatory paths of bodies freely rising or falling in fluids, Annu. Rev. Fluid Mech. **44**, 97 (2012).

[14] W. W. Willmarth, N. E. Hawk, and R. L. Harvey, Steady and unsteady motions and wakes of freely falling disks, Phys. Fluids **7**, 197 (1964).

[15] S. B. Field, M. Klaus, M. Moore, and F. Nori, Chaotic dynamics of falling disks, Nature (London) **388**, 252 (1997).

[16] H. Zhong, C. Lee, Z. Su, S. Chen, M. Zhou, and J. Wu, Experimental investigation of freely falling thin disks. Part 1. The flow structures and Reynolds number effects on the zigzag motion, J. Fluid Mech. **716**, 228 (2013).

[17] C. Lee, Z. Su, H. Zhong, S. Chen, M. Zhou, and J. Wu, Experimental investigation of freely falling thin disks. Part 2. Transition of three-dimensional motion from zigzag to spiral, J. Fluid Mech. **732**, 77 (2013).

[18] F. Auguste, J. Magnaudet, and D. Fabre, Falling styles of disks, J. Fluid Mech. **719**, 388 (2013).

[19] L. Heisinger, P. Newton, and E. Kanso, Coins falling in water, J. Fluid Mech. **742**, 243 (2014).

[20] T. Kim, J. Chang, and D. Kim, Free-fall dynamics of a pair of rigidly linked disks, Phys. Fluids **30**, 034104 (2018).

[21] M. Lee, S. H. Lee, and D. Kim, Stabilized motion of a freely falling bristled disk, Phys. Fluids **32**, 113604 (2020).

[22] X. Zhou, S. Yuan, and G. Zhang, Eccentric disks falling in water, Phys. Fluids **33**, 033325 (2021).

[23] G. Verhille, Deformability of discs in turbulence, J. Fluid Mech. **933**, A3 (2022).

[24] L. Esteban, J. Shrimpton, and B. Ganapathisubramani, Disks settling in turbulence, J. Fluid Mech. **883**, A58 (2020).

[25] M. M. Mrokowska, Stratification-induced reorientation of disk settling through ambient density transition, Sci. Rep. **8**, 412 (2018).

[26] M. Mercier, S. Wang, J. Péméja, P. Ern, and A. Ardekani, Settling disks in a linearly stratified fluid, J. Fluid Mech. **885**, A2 (2020).

[27] H. Moffatt, Three coins in a fountain, J. Fluid Mech. **720**, 1 (2013).

[28] G. Langdon, G. Nurick, V. Balden, and R. Timmis, Perforated plates as passive mitigation systems, Def. Sci. J. **58**, 238 (2008).

[29] S. Shaaban, On the performance of perforated plate with optimized hole geometry, Flow Meas. Instrum. **46**, 44 (2015).

[30] L. Lignarolo, D. Ragni, C. Ferreira, and G. Van Bussel, Experimental comparison of a wind-turbine and of an actuator-disc near wake, J. Renewable Sustainable Energy **8**, 023301 (2016).

[31] H. Higuchi, J. Zhang, S. Furuya, and B. K. Muzas, Immediate and near wake flow patterns behind slotted disks, AIAA J. **36**, 1626 (1998).

[32] R. Theunissen and R. Worboys, Near-wake observations behind azimuthally perforated disks with varying hole layout and porosity in smooth airstreams at high Reynolds numbers, J. Fluids Eng. **141**, 051108 (2019).

[33] L. Vincent, W. S. Shambaugh, and E. Kanso, Holes stabilize freely falling coins, J. Fluid Mech. **801**, 250 (2016).

[34] D. Bi, Y. Wei, C. Wang, and H. Xu, Experimental study on the vortex structure and path instability of freely falling annular disks, Sci. China Technol. Sci. **61**, 853 (2018).

[35] D. Bi, Y. Wei, R. Theunissen, and H. Xu, Study on the flow structure behind a freely falling annular disk using proper orthogonal decomposition, Eur. J. Mech. B Fluids **85**, 90 (2021).

[36] V. Iyer, H. Gaensbauer, T. L. Daniel, and S. Gollakota, Wind dispersal of battery-free wireless devices, Nature **603**, 427 (2022).

[37] H.-J. Zhong and C.-B. Lee, The wake of falling disks at low Reynolds numbers, Acta Mech. Sin. **28**, 367 (2012).

[38] P. Romero-Gomez and M. C. Richmond, Numerical simulation of circular cylinders in free-fall, J. Fluids Struct. **61**, 154 (2016).

[39] L. Liu, J. Yang, H. Lu, X. Tian, and W. Lu, Numerical simulations on the motion of a heavy sphere in upward poiseuille flow, Ocean Eng. **172**, 245 (2019).

[40] A. Shenoy and C. Kleinstreuer, Flow over a thin circular disk at low to moderate Reynolds numbers, J. Fluid Mech. **605**, 253 (2008).

[41] X. Tian, L. Xiao, X. Zhang, J. Yang, L. Tao, and D. Yang, Flow around an oscillating circular disk at low to moderate Reynolds numbers, J. Fluid Mech. **812**, 1119 (2017).

[42] K. Watanabe and K. Matsuno, Moving computational domain method and its application to flow around a high-speed car passing through a hairpin curve, J. Comput. Sci. Technol. **3**, 449 (2009).

[43] A. Shenoy and C. Kleinstreuer, Influence of aspect ratio on the dynamics of a freely moving circular disk, J. Fluid Mech. **653**, 463 (2010).

[44] F. W. Roos and W. W. Willmarth, Some experimental results on sphere and disk drag, AIAA J. **9**, 285 (1971).

[45] See Supplemental Material at http://link.aps.org/supplemental/10.1103/PhysRevFluids.7.054702 for the sequences of 3D trajectories, flow structures, and time evolutions of the kinematic and dynamic parameters for the disks at different falling patterns.

[46] B. Cabral and L. C. Leedom, Imaging vector fields using line integral convolution, in *Proceedings of the 20th Annual Conference on Computer Graphics and Interactive Techniques (SIGGRAPH)* (Anaheim, CA, 1993), pp. 263–270.

[47] K. Namkoong, J. Y. Yoo, and H. G. Choi, Numerical analysis of two-dimensional motion of a freely falling circular cylinder in an infinite fluid, J. Fluid Mech. **604**, 33 (2008).

[48] H. Ghassemi and E. Yari, The added mass coefficient computation of sphere, ellipsoid and marine propellers using boundary element method, Pol. Marit. Res. **18**, 17 (2011).

[49] J. N. Newman, *Marine Hydrodynamics* (MIT Press, Cambridge, MA, 2018).

[50] J. Sherwood and H. A. Stone, Added mass of a disc accelerating within a pipe, Phys. Fluids **9**, 3141 (1997).

[51] J. Sherwood, Added mass of a pair of discs, Phys. Fluids **23**, 103601 (2011).

[52] C. J. Tranter, *Bessel Functions with Some Physical Applications* (English Universities Press London, London, 1968).

[53] M. Rahmani and A. Wachs, Free falling and rising of spherical and angular particles, Phys. Fluids **26**, 083301 (2014).

[54] A. Seyed-Ahmadi and A. Wachs, Dynamics and wakes of freely settling and rising cubes, Phys. Rev. Fluids **4**, 074304 (2019).